Journal of Colloid and Interface Science 440 (2015) 168–178

Contents lists available at ScienceDirect

Journal of Colloid and Interface Science

www.elsevier.com/locate/jcis

Capillary meniscus dynamometry – Method for determining the surface tension of drops and bubbles with isotropic and anisotropic surface stress distributions

Krassimir D. Danov [a], Rumyana D. Stanimirova [a], Peter A. Kralchevsky [a,*], Krastanka G. Marinova [a], Nikola A. Alexandrov [a], Simeon D. Stoyanov [b,c,d], Theodorus B.J. Blijdenstein [b], Eddie G. Pelan [b]

[a] Department of Chemical Engineering, Faculty of Chemistry and Pharmacy, Sofia University, Sofia 1164, Bulgaria
[b] Unilever Research & Development Vlaardingen, 3133AT Vlaardingen, The Netherlands
[c] Laboratory of Physical Chemistry and Colloid Science, Wageningen University, 6703 HB Wageningen, The Netherlands
[d] Department of Mechanical Engineering, University College London, WC1E 7JE, UK

ARTICLE INFO

Article history:
Received 25 August 2014
Accepted 25 October 2014
Available online 7 November 2014

Keywords:
Pendant drops and buoyant bubbles
Protein adsorption layers
Anisotropic interfacial layers
Drop shape analysis
Surface stress balances
Non-uniform surface tension

ABSTRACT

The stresses acting in interfacial adsorption layers with surface shear elasticity are, in general, anisotropic and non-uniform. If a pendant drop or buoyant bubble is covered with such elastic layer, the components of surface tension acting along the "meridians" and "parallels", σ_s and σ_φ, can be different and, then, the conventional drop shape analysis (DSA) is inapplicable. Here, a method for determining σ_s and σ_φ is developed for axisymmetric menisci. This method, called 'capillary meniscus dynamometry' (CMD), is based on processing data for the digitized drop/bubble profile and capillary pressure. The principle of the CMD procedure for data processing is essentially different from that of DSA. Applying the tangential and normal surface stress balance equations, σ_s and σ_φ are determined in each interfacial point without using any rheological model. The computational procedure is fast and could be used in real time, during a given process. The method is applied to determine σ_s and σ_φ for bubbles and drops formed on the tip of a capillary immersed in solutions of the protein HFBII hydrophobin. Upon a surface compression, meridional wrinkles appear on the bubble surface below the bubble "equator", where the azimuthal tension σ_φ takes negative values. The CMD method allows one to determine the local tensions acting in anisotropic interfacial layers (films, membranes), like those formed from proteins, polymers, asphaltenes and phospholipids. The CMD is applicable also to fluid interfaces (e.g. surfactant solutions), for which it gives the same surface tension as the conventional methods.

1. Introduction

Interfacial layers from proteins [1–9]; saponins [10]; polymers, polyelectrolytes and their mixtures with proteins [11–13]; phospholipids [14,15]; particles [16,17] and asphaltenes [18], can possess surface shear elasticity, i.e. they can behave as a two-dimensional elastic solid (membrane). In general, the stresses acting in such layers are anisotropic and non-uniform – they vary along the interface [19–23]. If a pendant drop (or buoyant bubble) is covered with an elastic interfacial layer, the components of surface tension acting along the "meridians" and "parallels", σ_s and σ_φ, can be rather different. In such a case, the conventional drop shape analysis (DSA) method [24], which presumes uniform and isotropic surface tension, is inapplicable. With such systems, at sufficiently high surface anisotropy the DSA apparatus shows a significant increase in the error of the Laplace fit of the drop/bubble profile [25,26].

To overcome this problem, here a method for anisotropic interfaces, i.e., for determining σ_s and σ_φ in each point, is developed for axisymmetric menisci. The method is based on obtaining and processing experimental data for the digitized drop/bubble profile and for the pressure difference across the meniscus. Such data can be obtained by upgrading a DSA setup with a pressure transducer. The computational procedure for determining σ_s and σ_φ in each point of the surface is essentially different from that used in DSA to determine a single surface tension σ for the whole meniscus.

Despite the non-uniform surface stress distribution and the different computational procedure, the present study can be considered as an extension of the known pendant drop and DSA methods, which are generalized for the case of *anisotropic* stresses here.

* Corresponding author. Fax: +359 2 9625643.
E-mail address: pk@lcpe.uni-sofia.bg (P.A. Kralchevsky).

http://dx.doi.org/10.1016/j.jcis.2014.10.067
0021-9797/

The first quantitative and methodological study on the profile of axisymmetric drops was carried out by Bashforth and Adams [27], who tabulated the profiles of sessile drops. Andreas et al. [28] are the authors of the pendant drop method, where σ is determined from specific meniscus dimensions; see Ref. [29] for detailed review. After the invention of the computer image analysis, Rotenberg et al. [24] made the revolutionary step to an almost complete automation of the pendant drop method by numerical fitting of the digitized drop profile with the Laplace equation of capillarity. This method, called axisymmetric drop shape analysis (ADSA), or more briefly DSA, has found a wide application for the measurements of static and dynamic surface tension and interfacial rheology [30–32]. The accuracy of surface tension measurements and the role of image analysis have been investigated in Refs. [33,34].

Another approach for determining σ for isotropic fluid interface is based on the measurements of the *capillary pressure* and curvature radius of a small non-deformed spherical drop (meniscus) protruding at the tip of a capillary tube. In the first realizations of this method, called capillary pressure tensiometry (CPT), image analysis has not been used – the drop radius at each moment is calculated from the known volume dosing rate [35–37]. The CPT has different versions and realizations and it is widely used to measure the static and dynamic surface tension and dilatational interfacial rheology [32,38,39]. Assembling of CPT and DSA in one apparatus combines the capabilities of both techniques [40–42].

In the more complex case of *anisotropic* surface stresses (tensions) considered here, we combine image analysis with capillary pressure measurements. As already mentioned, anisotropic stresses are observed with solid (non-fluid) interfaces. Here and hereafter we are using the term "solid" (or "solidification") for an interfacial layer (membrane) that possesses surface shear elasticity. We have in mind an elastic solid, rather than a non-deformable solid.

The paper is organized as follows. In Section 2 we consider the two basic equations used in this study, which represent projections of the vectorial surface stress balance along the "meridian" and along the normal to the axisymmetric meniscus. (The force balance along the "parallel" is trivial because of the axial symmetry). Section 3 is central for the present study – it describes the principle of the computational procedure, which is essentially different from that of DSA, and is based on the use of a first integral of the surface stress balance equations. Next, the proposed method is tested against data for pendant drops and buoyant bubbles in aqueous solutions of the protein hydrophobin HFBII. Section 4 describes the used materials and experimental methods, including the determination of capillary pressure. In Section 6, the method is first tested against data for pendant drops with fluid interfaces, and next – for a buoyant bubble with solidifying surface in a HFBII solution at different stages of bubble shrinkage. The two surface tensions, σ_s and σ_φ, are determined as functions of the position on the bubble surface. At a larger degree of shrinkage, meridional wrinkles appear in a certain zone of the bubble surface, where the azimuthal tension σ_φ takes negative values.

The method developed here, called capillary meniscus dynamometry (CMD), is applicable to determine both static and dynamic values of σ_s and σ_φ for axisymmetric menisci (e.g. drops and bubbles) with anisotropic surface stresses. A simpler version of the method (without capillary pressure measurements) is applicable also to the special case of isotropic surfaces.

In preceding studies on anisotropic interfacial layers [19–23], the Hookean or neo-Hookean model of elastic plates is used from the very beginning. In this respect, the approach in the present article is essentially different. The method proposed here allows one to *directly* determine the two surface tensions, σ_s and σ_φ, in each point of the drop/bubble surface from experimental data, without using any model assumptions. At a next step (out of the scope of this study), one could construct a rheological model to interpret the behavior of σ_s and σ_φ for each separate specific system. The constructed models would be much more realistic if the variations of σ_s and σ_φ along the bubble/drop surface, and the reference isotropic initial state have been determined in advance, by using the method proposed in the present article.

2. Surface stress balances for an axisymmetric meniscus

2.1. Basic equations

Let us consider an axisymmetric meniscus, like the surface of a pendant drop sketched in Fig. 1a. To describe its shape, we will use cylindrical coordinates (r, φ, z), with coordinate origin at the meniscus apex, i.e. at the point where the z-axis pierces the interface; r is the radial coordinate and φ is the azimuthal angle. The generatrix of the meniscus profile can be parameterized with the length of the arc, s:

$$\frac{dr}{ds} = \cos\theta \quad \text{and} \quad \frac{dz}{ds} = \sin\theta \tag{1}$$

where θ is the running meniscus slope angle. The pair (s, φ) represents a system of orthogonal coordinates on the axisymmetric meniscus. Because of the axial symmetry, the surface stress tensor has two components, σ_s and σ_φ, which are tangential, respectively, to the s and φ coordinate lines (Fig. 1a).

At equilibrium, the balance of linear momentum in each point of the meniscus has two non-zero projections, which represent relations between σ_s and σ_φ, [23,43,44]:

$$\sigma_\varphi = \frac{d}{dr}(\sigma_s r) \quad \text{(tangential projection)} \tag{2}$$

$$\kappa_s\sigma_s + \kappa_\varphi\sigma_\varphi = p_s \quad \text{(normal projection)} \tag{3}$$

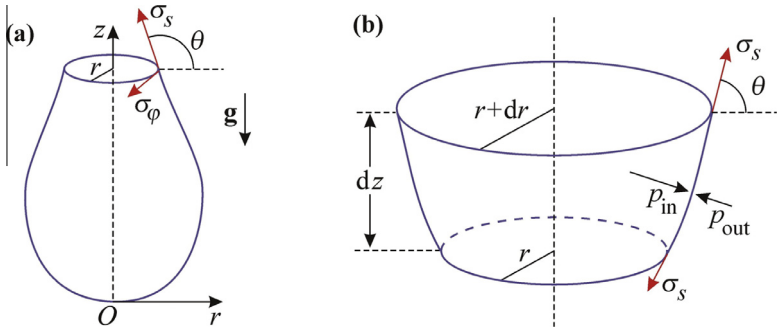

Fig. 1. (a) Sketch of a pendant drop; σ_s and σ_φ are two components of surface tension acting along the "meridians" and "parallels". The vertical resultant of the surface tension force, $2\pi r\sigma_s \sin\theta$, is counterbalanced by the pressure force F_p; see Eq. (11). (b) An element of the meniscus profile of height dz.

p_s is the local pressure difference along the meniscus, whereas κ_s and κ_φ are the respective two principal curvatures:

$$\kappa_s = \frac{d\theta}{ds} \quad \text{and} \quad \kappa_\varphi = \frac{\sin\theta}{r} \tag{4}$$

Eq. (3) is a form of the Laplace equation of capillarity generalized for an anisotropic interface.

Here, we consider only surface tensions acting tangentially to the interface (membrane). In the case of objects of high curvature and low membrane tensions, the transverse shear stress resultants and the related interfacial bending moments (torques) should be taken into account [14,43,44]. The bending-moment effects are out of the scope of the present study, because here we are dealing with millimeter-sized drops and bubbles.

If the surface tension is uniform, then $d\sigma_s/dr = 0$ and Eq. (2) reduces to $\sigma_\varphi = \sigma_s$. In other words, if the surface tension is *uniform*, the balance of the linear momentum implies that it is also *isotropic*: $\sigma_\varphi = \sigma_s = \sigma$. This statement can be generalized to an arbitrarily curved interface with a symmetric surface stress tensor, viz. if the surface stresses are isotropic, they are also uniform throughout the interface, and *vice versa*. The proof of this more general statement is given in Appendix A, whereas the derivation of Eqs. (2) and (3) for the special case of axisymmetric interface – in Appendix B.

Substituting σ_φ, κ_s and κ_φ from Eqs. (2) and (4) into Eq. (3), in view of Eq. (1) one derives:

$$\frac{d}{dr}(\sigma_s r\sin\theta) = p_s r \tag{5}$$

See Appendix B for details. In general, σ_s can vary along the generatrix of the meniscus. σ_s is constant along the φ-lines because of the axial symmetry. If σ_s is completely constant (independent of r), then Eq. (5) reduces to the conventional Laplace equation [24,43,44].

2.2. Force balances at the drop/bubble

Because Eq. (5) lies in the basis of the CMD method, it is helpful to discuss its physical meaning in more details. For this goal, here Eq. (5) is derived by force-balance considerations.

Let us consider a layer from the drop/bubble of elementary thickness dz; see Fig. 1b. The z-projections of the forces acting on this elementary volume are:

$$2\pi r(\sigma_s\sin\theta)|_r + 2\pi r dr p_{\text{in}} = 2\pi(r+dr)(\sigma_s\sin\theta)|_{r+dr} + 2\pi r dr p_{\text{out}} \tag{6}$$

The forces in the left-hand side of Eq. (6) are directed downwards, whereas those in the right-hand side – upwards (Fig. 1b). Division of Eq. (6) by $2\pi dr$, followed by a limiting transition $dr \to 0$, leads to Eq. (5) with

$$p_s \equiv p_{\text{in}} - p_{\text{out}} = p_0 - \varepsilon g z \Delta\rho \tag{7}$$

In Eq. (7), we have taken into account the effect of the gravitational hydrostatic pressure, where p_0 is the pressure difference across the meniscus at level $z = 0$ (at the apex); $\Delta\rho \equiv \rho_{\text{in}} - \rho_{\text{out}}$ is the difference between the mass densities of the inner and outer phases; g is the magnitude of the acceleration due to gravity; $\varepsilon = 1$ if the z-axis is directed opposite to the gravity acceleration vector $\mathbf{g}$ (for pendant drops, as in Fig. 1a) and $\varepsilon = -1$ in the opposite case (for buoyant drops and bubbles).

Integrating Eq. (5), along with Eq. (7), with respect to r and multiplying by 2π, we obtain:

$$2\pi r\sigma_s\sin\theta = \pi r^2 p_0 - 2\pi\varepsilon g\Delta\rho\int_0^r \tilde{r}z(\tilde{r})d\tilde{r} \tag{8}$$

where $\tilde{r}$ is an integration variable. The left-hand side of Eq. (8) represents the z-projection of the *surface-tension force* acting on a cross-section of the meniscus at a given z (Fig. 1a). The right-hand side of Eq. (8), which represents the pressure difference integrated over the meniscus, is denoted F_p hereafter:

$$F_p \equiv \pi r^2 p_0 + \pi\varepsilon g\Delta\rho(I - r^2 z) \tag{9}$$

$$I = \int_0^z r^2(\tilde{z})d\tilde{z} \tag{10}$$

In Eq. (9), integration by parts has been used; I is an integral, which is calculated numerically. In view of Eq. (9), we can represent Eq. (8) in the form:

$$F_p = 2\pi r\sigma_s\sin\theta \tag{11}$$

In our experiments, we determine p_0 and the meniscus profile $r(z)$. As explained in the next section, from these data one can determine $F_p(z)$ and $\theta(z)$ for each given z. Then, the local value of the *meridional* tension σ_s can be determined from Eq. (11):

$$\sigma_s(z) = \frac{F_p(z)}{2\pi r(z)\sin\theta(z)} \tag{12}$$

Next, in view of Eqs. (1) and (4) the local values of the two principle curvatures are:

$$\kappa_\varphi(z) = \frac{\sin\theta(z)}{r(z)}, \quad \kappa_s(z) = -\frac{d\cos\theta(z)}{dz} \tag{13}$$

The derivative in the last equation is calculated numerically, as explained in the next section. Finally, using Eqs. (3) and (7) we determine the local value of the *azimuthal* tension σ_φ:

$$\sigma_\varphi(z) = \frac{p_0 - \varepsilon g z\Delta\rho - \kappa_s(z)\sigma_s(z)}{\kappa_\varphi(z)} \tag{14}$$

Thus, the local values of the two surface tensions, $\sigma_s(z)$ and $\sigma_\varphi(z)$, can be determined throughout the whole meniscus directly from the experimental data using the surface force balance equations. No model assumptions regarding the rheological behavior of the interfacial layer are used. The key is the determination of the dependencies $F_p(z)$, $\theta(z)$ and $\kappa_s(z)$ from the experimental data, which is described in the next section.

3. Determination of the local values of surface tension from experimental data

From the digitized profile of a pendant drop (or buoyant bubble) one can determine the experimental dependence $r^2(z)$, which appears under the integral in Eq. (10). As an illustration, Fig. 2 shows a typical experimental $r^2(z)$ dependence for a pendant drop of water.

First the digitalized images are transformed from pixels to physical Cartesian coordinates (r_k, z_k) of the points from the drop/bubble profile. For the microscope magnification used in our experiments, one pixel is equal to 12 μm. Next, the algorithm includes (i) determination of the position of the symmetry axis, which does not necessarily coincide with the vertical axis of the experimental video frames (the camera is usually slightly tilted); (ii) rotation of the profile to have the z-axis of the Cartesian coordinate system directed along the axis of symmetry; (iii) calculation of the position of drop (bubble) apex in the new coordinate system; (iv) transformation of the Cartesian coordinates to cylindrical ones with origin at the drop/bubble apex. As a result, the left and right profiles of the drop (bubble) overlap when plotted in (r, z) coordinates. The $r^2(z)$ plot in Fig. 2 has been obtained as a result of this procedure.

Furthermore, the region of variation of z is divided to n equal parts (20 parts in the illustrative Fig. 2 and 72 parts for the buoyant bubbles in Section 5.2):

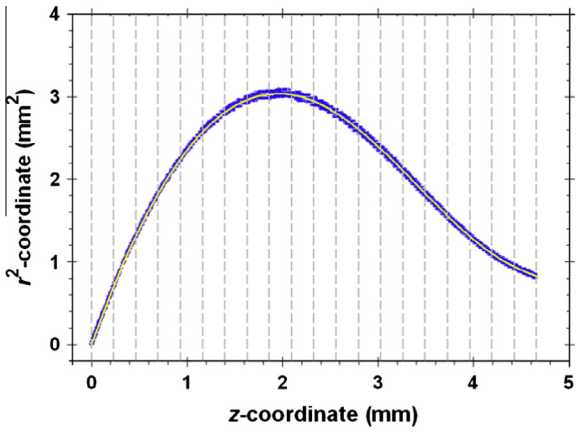

Fig. 2. Experimental meniscus profile of a pendant water drop (the dots). The solid line represents the set of all interpolation curves by Eq. (16) in all $[z_{j-1}, z_j]$ intervals ($j = 1, \ldots, n$), which are confined between two neighboring vertical dashed lines.

$$z_{j-1} \le z \le z_j, \quad j = 1, \ldots, n \tag{15}$$

Because of the small pixel size, each interval in Eq. (15) contains a large number of experimental (r_k, z_k) points. In each of these intervals, the experimental $r^2(z)$ dependence is fitted with a second-order polynomial:

$$r^2 = a_j z^2 + b_j z + c_j \quad (z_{j-1} \le z \le z_j) \tag{16}$$

Thus, the coefficients a_j, b_j, and c_j are determined as adjustable parameters by using the least squares method. The local value of the meniscus slope angle θ can be estimated from the expression:

$$\cot\theta = \frac{dr}{dz} = \frac{2a_j z + b_j}{2r} \tag{17}$$

Further, we obtain:

$$\sin\theta = (1 + \cot^2\theta)^{-1/2} = \left[1 + \left(\frac{2a_j z + b_j}{2r}\right)^2\right]^{-1/2} \tag{18}$$

$$\cos\theta = \pm(1 + \tan^2\theta)^{-1/2} = \frac{2a_j z + b_j}{\left[4r^2 + (2a_j z + b_j)^2\right]^{1/2}} \tag{19}$$

In view of Eq. (13), we differentiate Eq. (19), along with Eq. (16), to obtain an expression for the meridional curvature:

$$\kappa_s(z) = -\frac{d\cos\theta(z)}{d\,z} = \frac{2(b_j^2 - 4a_j c_j)}{\left[4r^2 + (2a_j z + b_j)^2\right]^{3/2}} \tag{20}$$

For the middle point of each $[z_{j-1}, z_j]$ interval we define the quantity

$$\zeta_j = \frac{z_{j-1} + z_j}{2}, \quad j = 1, \ldots, n \tag{21}$$

Then, the value I_j of the integral I in each $[z_{j-1}, z_j]$ interval can be calculated from the following recurrence formula (see Eq. (10)):

$$I_1 = \int_0^{\zeta_1} r^2(z)d\,z = \frac{1}{3}a_1\zeta_1^3 + \frac{1}{2}b_1\zeta_1^2 + c_1\zeta_1 \tag{22}$$

$$I_j = \int_0^{\zeta_j} r^2(z)dz = I_{j-1} + a_j\frac{\zeta_j^3 - \zeta_{j-1}^3}{3} + b_j\frac{\zeta_j^2 - \zeta_{j-1}^2}{2} + c_1(\zeta_j - \zeta_{j-1}) \tag{23}$$

$j = 2, 3, \ldots, n$. In view of Eq. (9), the value of the force F_p in the middle of each $[z_{j-1}, z_j]$ interval is:

$$F_p(\zeta_j) \equiv \pi r^2(\zeta_j)(p_0 - \varepsilon g\zeta_j\Delta\rho) + \pi\varepsilon g\Delta\rho I_j \tag{24}$$

Next, Eq. (12) is used to calculate the value of the *meridional* surface tension σ_s in the middle of each $[z_{j-1}, z_j]$ interval:

$$\sigma_s(\zeta_j) = \frac{F_p(\zeta_j)}{2\pi r(\zeta_j)\sin\theta(\zeta_j)} \tag{25}$$

Finally, the *azimuthal* surface tension σ_φ (ζ_j) is calculated from Eqs. (13) and (14). There, as well as in Eqs. (24) and (25), the quantities $r(\zeta_j)$, $\sin\theta(\zeta_j)$ and $\kappa_s(\zeta_j)$ are given, respectively, by Eqs. (16), (18) and (20) with $z = \zeta_j$. The pressure p_0 in Eq. (24) is supposed to be determined by the pressure transducer measurements as explained in Section 4.2.

4. Experimental section

4.1. Materials and methods

To test the above method for determining σ_s and σ_φ, we carried out experiments with buoyant bubbles is aqueous solutions of the protein HFBII (received from Unilever), which is a class II hydrophobin of molecular mass 7.2 kDa. HFBII is composed from 70 amino acids with 4 disulfide bonds. It is a relatively small and compact protein molecule, which is stable (does not denature) upon heating up to 90 °C and upon adsorption on air/water and solid/water interfaces [45]. At the air/water and oil/water interfaces, HFBII forms rigid adsorption layers that exhibit surface shear elasticity [5–8,46,47]. In such a case, σ_s and σ_φ are different and vary from point to point throughout the bubble (or drop) surface.

In comparative experiments, we used pendant drops from deionized water of specific resistivity 18.2 MΩ cm (Elix purification system, Millipore). 3 mM NaCl (Merk) were added to the aqueous phase to have a defined ionic strength. In other comparative experiments we used pendant drops from a solution of sodium dodecyl sulfate (SDS), product of Acros Organics (Pittsburgh, PA). All experiments were carried out at a room temperature of 25 ± 1 °C.

In the measurements with drops and bubbles, we used the setup for capillary pressure tensiometry (CPT) described in Ref. [40]. It is a DSA10 apparatus (Krüss GmbH, Hamburg, Germany) upgraded with a pressure transducer (model PX163-2.5BD5V) to register the variations of pressure inside the drop/bubble with time. For a precise increase and decrease of the drop/bubble volume, a piezo-driven membrane was used.

4.2. Determination of the reference capillary pressure p_0

By definition, p_0 is the capillary pressure difference across the drop/bubble apex (at $z = 0$); see Fig. 1a and Eq. (7). However, the pressure transducer measures the pressure difference, p_{tr}, at a different level. The relation between p_0 and p_{tr} depends on whether we are dealing with pendant drop (Fig. 3a) or buoyant bubble (Fig. 3b).

4.2.1. Pendant drop

In the case of pendant drop in air, the capillary is filled with the working solution. In such case, the pressure difference is due to the hydrostatic pressure between the levels of the apex and the transducer:

$$p_0 = p_{tr} + \rho_{in}g(H + h) \tag{26}$$

See Fig. 3a for the notations. The height of the drop, h, is measured directly from the digitized profile. To accurately determine H, we formed a small *spherical* drop (of height $h \ll H$) at the tip of the capillary and increased its volume by small steps, simultaneously measuring p_{tr} and the drop curvature radius R at each step. Next, the obtained data were plotted as p_{tr} vs. $2/R$ in accordance with the equation:

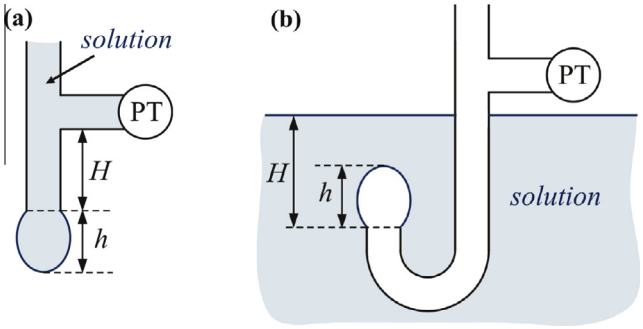

Fig. 3. Illustration of the determination of capillary pressure at the apex, p_0, from the pressure difference p_{tr} measured by a pressure transducer (denoted PT) for (a) pendant drop and (b) buoyant bubble.

$$p_{tr} = \frac{2\sigma}{R} - \rho_{in} g H \tag{27}$$

The intercept of this plot yields H. Because the distance H between the pressure transducer and the edge of the capillary is independent of the working solution, H was determined with pure water or a solution of a fast adsorbing surfactant, so that σ in Eq. (27) is the isotropic surface tension of this solution.

4.2.2. Buoyant bubble

In this case, the capillary is filled with air. Then, the transducer registers the pressure difference at the apex, p_0, plus the hydrostatic pressure *difference* between the level of the apex and the level of the flat air/solution interface (Fig. 3b). Hence, p_0 and p_{tr} are related as follows:

$$p_0 = p_{tr} - \rho_{out} g (H - h) \tag{28}$$

where ρ_{out} is the solution's density. To minimize the contribution of the last gravitational term in Eq. (28), the difference $H - h$ was decreased by placing the bubble close to the solution's surface.

During the experiment with a given drop or bubble, p_{tr} is measured as a function of time. Thus, the value of p_{tr} is known for each video frame of the drop/bubble profile, which is processed to determine the surface tension (see below).

5. Experimental results and discussion

5.1. Pendant drops and buoyant bubbles with fluid interfaces

To test the procedure for data processing described in Section 3, we applied it to a pendant drop from deionized water (for the same drop, the r^2-vs.-z plot is shown in Fig. 2), and to a buoyant bubble in 100 mM aqueous SDS solution. In these cases, we expect that the interfaces are fluid and the surface tension should be uniform and isotropic, i.e. $\sigma_s = \sigma_\varphi = \sigma = \text{const}$. In view of Eq. (11), the plot of F_p vs. $2\pi r \sin\theta$ must be a straight line, which passes through the coordinate origin and has a slope equal to σ.

Each point in Fig. 4 corresponds to the local values $r(\zeta_j)$, $\sin\theta(\zeta_j)$ and $F_p(\zeta_j)$ determined from Eqs. (16), (18) and (24) for the midpoint, $z = \zeta_j$, of the interval $[z_{j-1}, z_j]$, $j = 1, \ldots, n$, for a given drop/bubble profile. The value of p_0 in Eq. (24) is experimentally determined by the pressure transducer as explained in Section 4.2. The data for both the water and SDS solution perfectly comply with straight lines through the coordinate origin (Fig. 4). The slopes yield $\sigma = 72.2$ and 36.0 mN/m, in full agreement with the surface tension values determined for the same solutions by the DSA and Wilhelmy plate methods. This result demonstrates that the proposed CMD method works very well for uniform isotropic (fluid) interfaces. The differences between the DSA and CMD methods are discussed in Section 5.3.

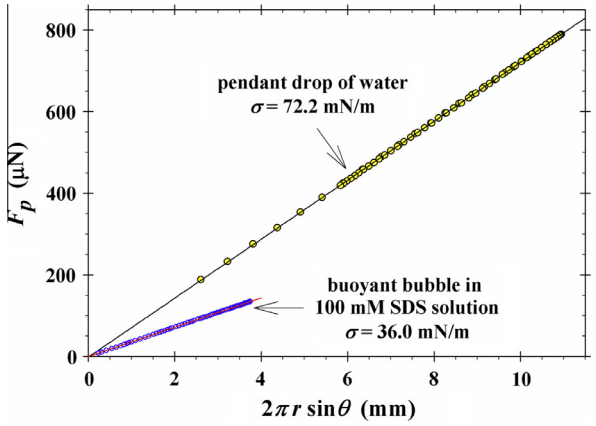

Fig. 4. Plot of F_p vs. $2\pi r\sin\theta$ for isotropic (fluid) interfaces: (i) pendant drop of water, and (ii) a smaller buoyant bubble in aqueous solution of 100 mM SDS. The values of σ shown in the graph are determined from the slope of the respective line in accordance with Eq. (11).

5.2. Bubbles with solidifying protein adsorption layers

We carried out experiments with bubbles formed on the tip of a J-shaped capillary (Fig. 3b) immersed in 0.005 wt% HFBII solution. Fig. 5a shows the variation of the pressure p_{tr} registered by the transducer. The evolution of the bubble profile was recorded by video camera during the experiment. The dashed lines in Fig. 5a correspond to the moments of the processed video frames in Fig. 5b. During this run, the pressure inside the bubble has been decreased three times by the experimentalist, which is seen as three steps in the $p_{tr}(t)$ dependence in Fig. 5a. Each of these decreases in pressure causes bubble shrinkage. For $t \geqslant 357$ s, equidistant meridional wrinkles are observed on the bubble surface, in a zone below the bubble "equator". These wrinkles are not seen well in Fig. 5b, but they are seen well by visual observation with microscope. For the photos in Fig. 5b, an appropriate illumination was used to provide a sharp bubble profile, which is further processed by the CMD method (Section 3).

At the chosen relatively low HFBII concentration, 0.005 wt%, the surface tension, σ, of the protein solution reaches its equilibrium value for $\leqslant 1$ min [25,48]. Initially, the interface is fluid (isotropic) and indications for surface solidification (rise of the error of the Laplace fit determined by DSA) are observed after the surface tension becomes $\leqslant 50$ mN/m [25,26]. A slight expansion or shrinkage of the bubble surface can, respectively, impede or promote the interfacial solidification; see Fig. C2 in Appendix C.

To check the situation with the bubble in Fig. 5, we applied the CMD procedure and plotted the obtained F_p vs. $2\pi r\sin\theta$ in accordance with Eq. (11); see Fig. 6. The straight lines in Fig. 6a and b indicate that at $t = 200$ and 300 s the protein adsorption layer is isotropic. In contrast, the plots in Figs. 6c and d indicate deviations from a straight line through the coordinate origin at $t = 320$ and 350 s. These deviations are smaller for the upper part of the bubble (above the "equator"), and more pronounced for the lower part of the bubble, near the capillary.

The slopes of the lines in Fig. 6a and b give an isotropic surface tension $\sigma_s = \sigma_\varphi = 60.0$ and 60.8 mN/m, respectively. For the bubbles corresponding to Fig. 6c and d, we used the full CMD procedure and determined the local values of σ_s and σ_φ from Eqs. (14) and (25). In Fig. 7a and b, the obtained σ_s and σ_φ are plotted vs. the vertical coordinate, z, with coordinate origin at the bubble apex. One sees that σ_s and σ_φ coincide only at the apex (the only point with isotropic curvature on the bubble profile), whereas for $z > 0$ the azimuthal tension σ_φ is systematically lower than σ_s. A comparison of the values of σ_s and σ_φ in Fig. 7a and b shows that

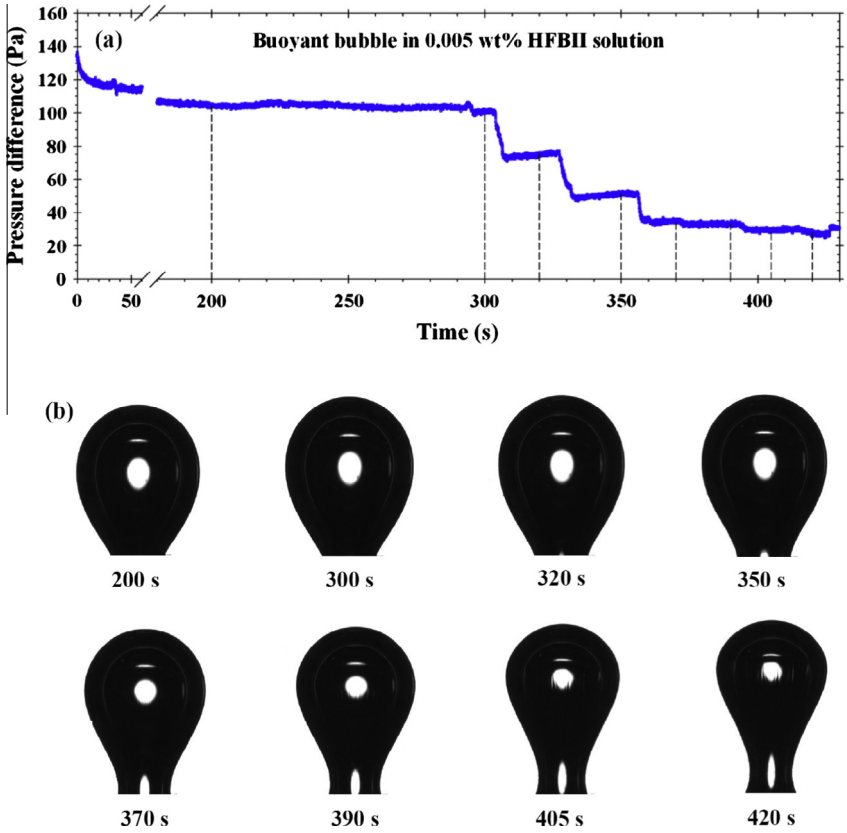

Fig. 5. (a) Plot of experimental data for the pressure p_{tr} vs. time t, see Eq. (28), for a buoyant bubble in 0.005 wt% HFBII solution. (b) Eight consecutive video frames of the bubble profile at different moments of time shown by vertical dashed lines in the p_{tr}-vs.-t plot.

the imposed bubble shrinkage at $t \approx 320$ s (Fig. 5a) has led to a significant lowering of both σ_s and σ_φ and to an increase of the difference between them (rise of surface anisotropy).

Fig. 7c–f shows the values of σ_s and σ_φ determined by CMD processing of the last four bubble profiles in Fig. 5b, that correspond to $t = 370$, 390, 405 and 420 s. As mentioned above, after the last forced bubble shrinkage at $t = 357$ s meridional wrinkles are observed on the bubble surface, below the bubble "equator". Fig. 7c–f shows that $\sigma_\varphi < 0$ in the region with wrinkles. This result is in agreement with the theoretical study on wrinkling upon unidirectional compression of elastic interfacial layers [49], where it has been established that wrinkles appear at negative values of the surface tension that is acting in direction perpendicular to the wrinkles. In our case, the wrinkles are directed along the meridians (the s-lines), and the azimuthal tension σ_φ takes negative values in the region of wrinkling.

A fluid interface may have only positive surface tension. In contrast, a solidified interfacial layer (a membrane possessing shear elasticity) may have either positive or negative tension when it is subjected, respectively, to stretching or compression, just like an elastic spring. The tension-free state (of zero tension) is in the middle between the aforementioned two regimes [14]. The membrane possesses an additional degree of freedom – to bend. In the region of negative tension, it is energetically more favorable the membrane to bend instead of to decrease its area upon compression [49]. This is the reason for the appearance of wrinkles. The bending elasticity (rigidity), k_c, determines the wavelength, λ, of the formed wrinkles. Conversely, the value of k_c can be obtained from the experimentally measured λ by using the formula $k_c = (\Delta\rho g\lambda^4)/(2\pi)^4$, which holds for a horizontal wrinkled interface; $\Delta\rho$ is the difference between the mass densities of the two adjacent fluid phases and g is the acceleration due to gravity; for details, see Refs. [49,50]. The determined values of σ_s and σ_φ in the zone with wrinkles (Fig. 7) represent average values of these two parameters. (The "microscopic" values of σ_s and σ_φ in this zone may oscillate as functions of the azimuthal angle φ.)

The registered difference between σ_s and σ_φ (Fig. 7) means that the interface has solidified, i.e., it possesses (non-zero) surface shear elasticity. However, the converse statement is not true. The interfacial layer may possess surface shear elasticity, but the surface stresses can be isotropic ($\sigma_s = \sigma_\varphi$) if the interface has been subjected to isotropic dilatation or compression. Hence, strictly speaking the straight lines in Fig. 6a and b imply that the surface stresses are isotropic, but they do not mean that the interfacial layer is fluid. One could determine whether the surface is fluid or solid by rotational rheometer, as in Refs. [5,7,8,46,47]. Another way is to compare the value of σ measured by DSA with the value $\sigma_{CMD}(0)$ determined by CMD at the drop apex, where $z = 0$; see Fig. C2 in Appendix C.

In summary, the results demonstrate that the CMD method enables one to determine the surface tensions in the cases of both isotropic (Fig. 6a and b) and anisotropic (Fig. 7) interface, including the cases with surface wrinkles (Fig. 7c–f).

5.3. Comparison of the DSA and CMD methods

The DSA method presumes the existence of a uniform and isotropic surface tension, σ. To determine σ, the bubble/drop profile is fitted with the Laplace equation

$$\frac{1}{r}\frac{d}{dr}(r\sin\theta) = \frac{p_0}{\sigma} - \varepsilon\frac{g\Delta\rho}{\sigma}z \tag{29}$$

Eq. (29) follows from Eqs. (5) and (7) for $\sigma_s = \sigma = \text{const}$. From computational viewpoint, it is convenient to use the length of the arc s

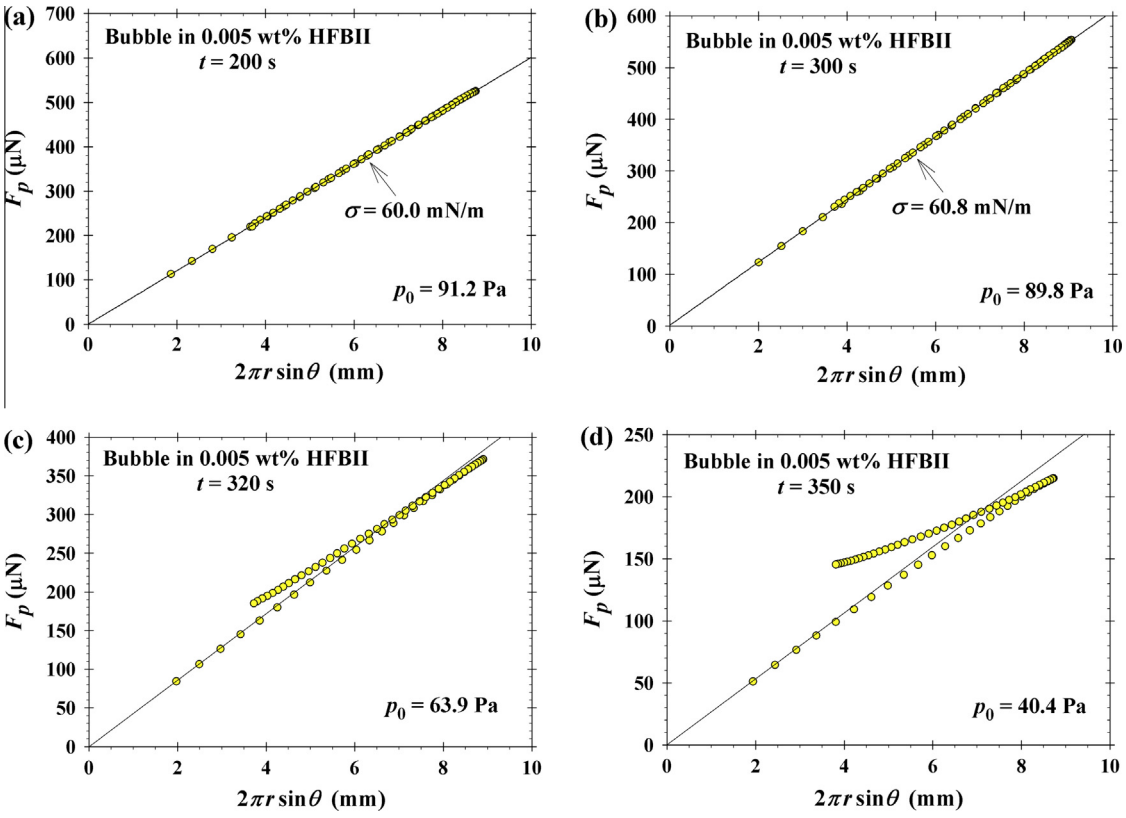

Fig. 6. Plots of F_p vs. $2\pi r\sin\theta$ for the first four bubble profiles in Fig. 5b: (a) t = 200 s; (b) t = 300 s; (c) t = 320 s; (d) t = 350 s. The straight lines at t = 200 and 300 s are the best fits with linear regression for isotropic interface in accordance with Eq. (11); the slope yields the value of σ denoted in the figure. The straight lines at t = 320 and 350 s visualize the deviations from linear dependence for these profiles.

as independent variable, and to calculate the functions $r(s)$, $z(s)$ and $\theta(s)$ by numerical integration of Eq. (29), together with Eq. (1); see e.g. Refs. [24,32,33]. The boundary conditions are $r(0) = 0$, $z(0) = 0$ and $\theta(0) = 0$. The two unknown parameters in Eq. (29), p_0 and σ, are determined as adjustable parameters from the fit of the data for the bubble/drop profile. An advantage of the DSA method is that it needs only a single set of data – that from the digitized drop profile. However, the DSA method is inapplicable to interfacial layers with anisotropic stresses, like those in Fig. 7.

The CMD method (Section 3) has been developed to determine the stresses acting in anisotropic interfacial layers. In addition to the digitized bubble/drop profile, the CMD needs also measurements of the capillary pressure p_0; see Section 4.2. The principle of the computational procedure of CMD is rather different from that of DSA. In DSA, the *whole* drop/bubble profile is fitted with the Laplace equation by using two adjustable parameters, viz. p_0 and σ. In contrast, no physical parameters are adjusted in CMD. The drop/bubble profile is divided to n small domains (Fig. 2) and in each of them the meniscus shape is fitted with a second order curve in accordance with Eq. (16). Then, a first integral of the surface stress balances is used to determine F_p and σ_s; see Eqs. (24) and (25). Furthermore, an analytical differentiation of the fitting curve is used to determine the meridional curvature κ_s in each domain, see Eq. (20), and finally, the azimuthal tension σ_φ is calculated from Eq. (14). In this way, the two independent surface stress balance equations, Eqs. (2) and (3), are employed to determine the meridional and azimuthal surface tensions σ_s and σ_φ locally, in each point of the interface; see Fig. 7.

The numerical procedure of CMD is fast and it has a fixed duration (for a given number of domains n), so that the method can be automated and applied to determine the dynamics of variation of σ_s and σ_φ in real time, during a given process, as well as for the creation of feedback that keeps, e.g., the bubble surface area constant during the experiment. In contrast, the duration of the numerical procedure of DSA depends on the degree of drop/bubble deformation, which affects the duration of the numerical minimization used to determine the adjustable parameters p_0 and σ. Note that for each pair of tentative values (p_0, σ), the Laplace equation has to be integrated numerically, which makes the DSA computational procedure slower than that of CMD. The adjustable parameters a_j, b_j and c_j in Eq. (16) are expressed *analytically* through the coordinates of the experimental points r_k and z_k (standard expressions of the least squares method for fit with a second-order polynomial [51]), so that CMD does not use numerical minimization.

The measured value of p_0 allows one to determine whether the interfacial stresses are isotropic or anisotropic, even at small deviations from isotropy. To demonstrate that, in Table 1 we compare results from the application of CMD and DSA to process the bubble profiles at t = 200, 300, 320 and 350 s in Fig. 5b; see also Fig. 6.

The first two columns of Table 1 contain the experimental values of t and p_0, the latter determined from the pressure-transducer measurement (Section 4.2). The third column shows the values of σ_s determined by CMD. For t = 200 and 300 s the surface stresses are isotropic and σ_s is determined from the slope of the lines in Fig. 6a and b. For t = 320 and 350 s, the stresses are anisotropic and σ_s varies in a certain range along the bubble profile as seen in Fig. 7a and b.

The fourth column in Table 1 shows the values of σ for the same bubble profiles determined by DSA. For the isotropic interfaces at t = 200 and 300 s, the values of σ determined by DSA practically coincide with those independently determined by CMD (in the third column). However, at t = 320 and 350 s, at which CMD yields non-uniform anisotropic stresses, DSA gives constant values of σ, which are greater than the greatest values of σ_s determined by

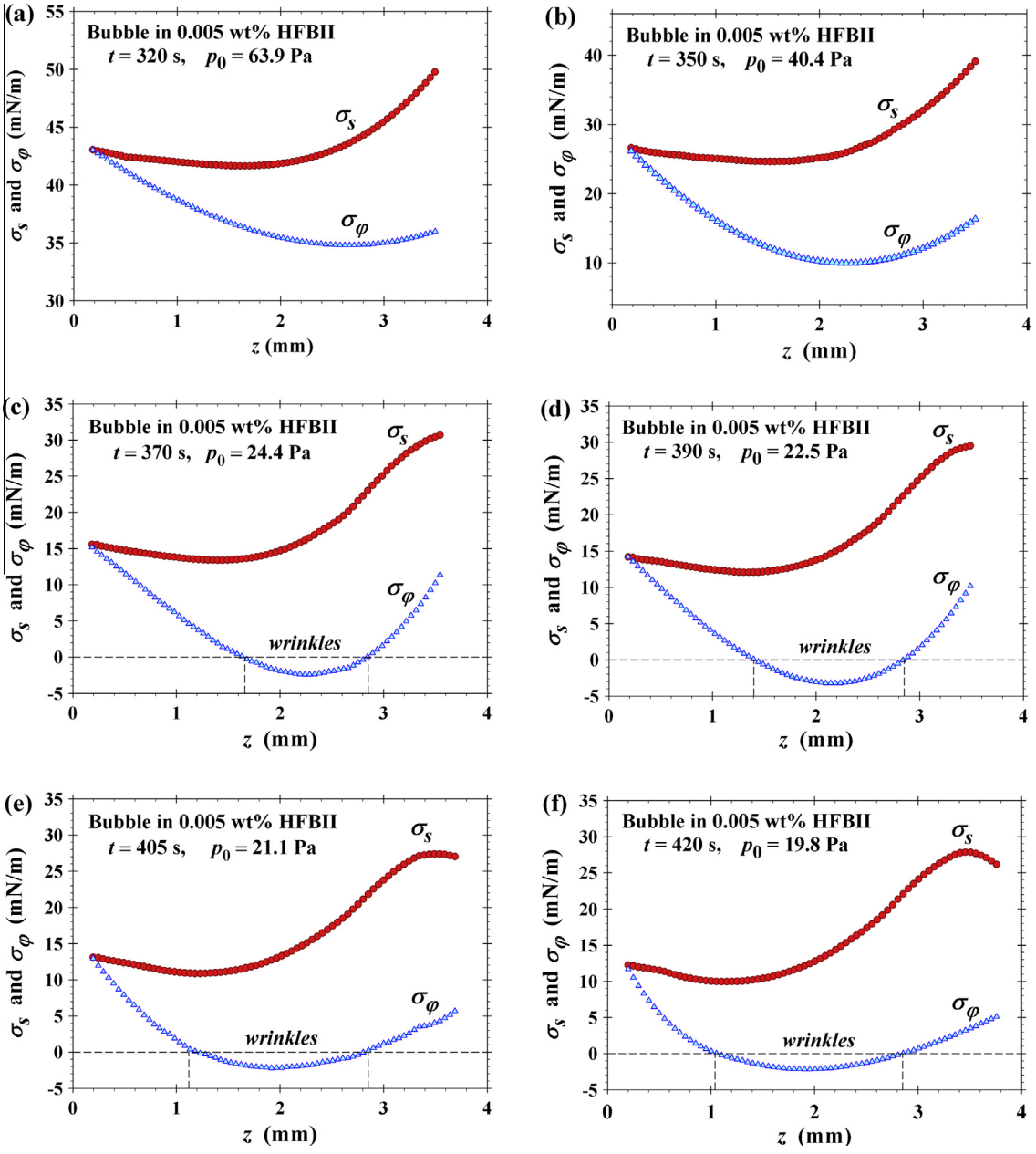

Fig. 7. Plots of the two components of surface tension, σ_s and σ_φ, vs. the z-coordinate for the bubbles with *anisotropic* surface tension in Fig. 5b: (a) $t = 320$ s; (b) $t = 350$ s; (c) $t = 370$ s; (d) $t = 390$ s; (e) $t = 405$ s; (f) $t = 420$ s; $z = 0$ at the bubble apex. The values of p_0 have been experimentally determined by pressure transducer. In the zone with $\sigma_\varphi < 0$, meridional wrinkles are observed on the bubble surface.

Table 1
Comparison of the values of σ_s and σ determined, respectively, by CMD and DSA from the first four bubble profiles in Fig. 5b.

t (s)	CMD with measured p_0		DSA	CMD with adjustable p_0	
	p_0 (Pa)	σ_s (mN/m)	σ (mN/m)	p_0 (Pa)	σ (mN/m)
200	91.2	60.0	60.0	91.1	60.0
300	89.8	60.8	60.6	90.0	60.8
320	63.9	41.7–49.7	57.7	86.7	57.8
350	40.4	24.6–38.1	57.0	85.4	56.7

CMD. At that, the error of the Laplace fit determined by the DSA apparatus is relatively small and does not indicate deviations from isotropy (see Fig. C1 in Appendix C). In contrast, CMD clearly indicates that the interface is anisotropic; see Figs. 6c, d and 7a, b. We could hypothesize that this discrepancy is due to the fact that DSA uses p_0 as a second adjustable parameter, instead of measuring p_0 as with CMD. Thus, the variation of two parameters, σ and p_0, can compensate the difference between the experimental and Laplace profiles at the cost of obtaining non-physical values of σ and p_0 with DSA.

To verify the above hypothesis, we processed the same bubble profiles with the CMD procedure, but this time p_0 in Eq. (24) was treated as an adjustable parameter, which was determined from the fit of the plot of F_p vs. $2\pi r\sin\theta$ with linear regression. The best fits for $t = 320$ and 350 s are shown in Fig. 8a, b, and the values of p_0 and σ obtained from all four fits are given in the last two columns of Table 1. As expected, the obtained values of σ practically coincide with those determined by DSA. However, for the anisotropic interfaces at $t = 320$ and 350 s the calculated p_0 is considerably higher than the experimental value of this parameter; compare the second and the fifth columns of Table 1.

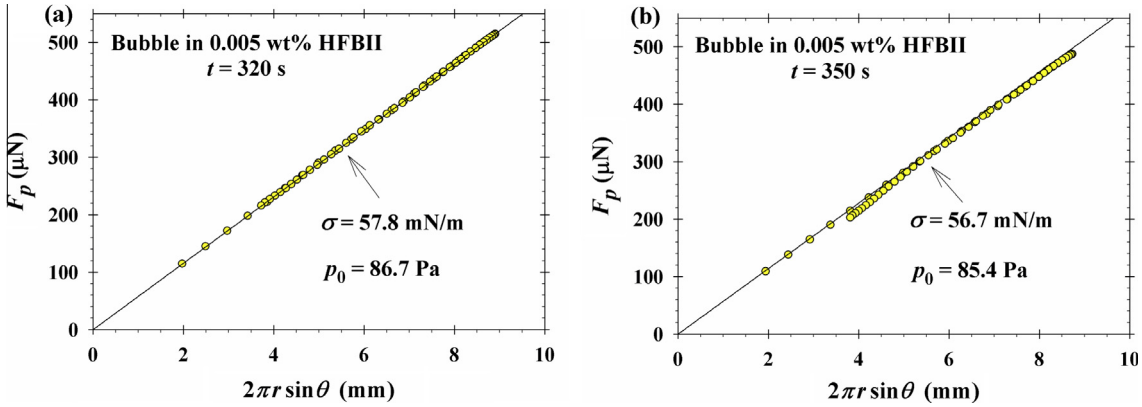

Fig. 8. Plots of F_p vs. $2\pi r\sin\theta$ for the best fits of the bubble profiles at (a) $t = 320$ s and (b) $t = 350$ s; σ and p_0 are determined as adjustable parameters and their values, corresponding to the best fit with Eq. (30), are given in the figures.

These results demonstrate that DSA can give incorrect values of σ for slightly anisotropic interfacial layers, assuming that the interface is isotropic and using σ and p_0, as two adjustable parameters. At higher degrees of anisotropy (at $t > 360$ s in Fig. C1 in Appendix C), the variation of the two adjustable parameters cannot compensate the difference between the experimental and Laplace profiles, and the DSA apparatus indicates a significant rise in the error of the Laplace fit. However, as demonstrated above, the error of the Laplace fit by DSA is insensitive to the smaller deviations from surface isotropy. For this reason, when working with solidifying interfacial layers (like those from proteins) it is safe to use CMD instead of DSA.

As demonstrated in Table 1 (the first two rows), the CMD approach (Section 3), which is based on splitting of the meniscus profile to $[z_{j-1}, z_j]$ intervals ($j = 1, \ldots, n$), and calculation of r_j, θ_j and I_j in the middle of each of them, can be applied to the special case of *isotropic* interface with two adjustable parameters, σ and p_0. In such case, Eqs. (9) and (11) can be represented in the form:

$$f = (2\pi r\sin\theta)\sigma - \pi r^2 p_0 \tag{30}$$

$$f \equiv \pi\varepsilon g\Delta\rho(I - r^2 z) \tag{31}$$

The values of f calculated for the midpoints of all $[z_{j-1}, z_j]$ intervals from Eq. (31) can be fitted with Eq. (30). Because in Eq. (30) f depends linearly on σ and p_0, the least squares method yields explicit analytical expressions for these two parameters [51], and thus the time-consuming numerical minimization, used in the DSA for Laplace fit, is avoided. In other words, for *isotropic* interfaces σ can be determined by the CMD procedure *only* from the digitized meniscus profile and fit with Eq. (30), *without* any pressure measurements. Table 1 (the first two rows) demonstrates that in this case CMD and DSA give the same σ. The quality of the fit can be illustrated with a plot like those in Figs. 4 and 6a, b.

The CMD can be applied to study the interaction of bubbles and drops with solid surfaces; see Appendix D. The CMD methodology (Section 3) could be also applied to obtain a detailed distribution of the surface stresses in experiments with the micropipette technique [52,53], which is dealing with axisymmetric model and biological phospholipid membranes, and where the pressure difference is also measured. For μm-sized vesicles and cells, the bending-moment effects (neglected here) could also become essential [54,55].

5.4. Discussion on the relation between CMD and the rheological models

An alternative approach to *anisotropic* interfaces exists, which is based on the postulation of a rheological model (relation between stress and strain) for an *elastic plate* from the very beginning [19–23]. In this approach, the drop/bubble profile is fitted with the theoretical shape predicted by the model, and its parameters (e.g. Young modulus and Poisson ratio) are determined from the best fit. Next, the two surface tensions, σ_s and σ_φ are calculated using the respective expressions in the framework of the model. This elastic-plate approach faces four difficulties, as follows.

(i) A reference state with isotropic stresses and zero (by definition) strain is needed, in order to quantify the strains and stresses upon subsequent deformations. However, the initial isotropic state is not *a priori* known, but it can be determined by CMD (see Fig. C2 in Appendix C).

(ii) The obtained σ_s and σ_φ would depend on the choice of the rheological model. In contrast, CMD yields unambiguous values of σ_s and σ_φ, which are determined directly from the experimental data.

(iii) If the interfacial deformation is not sufficiently slow, the surface *viscous* stresses would also become essential, in addition to the *elastic* ones. Then the rheological model would contain at least four parameters, surface dilatational and shear elastic and viscous moduli [56], and some of them may depend on the rate of strain; see e.g. Refs. [7,8,46,47]. This would result in a very hard mechanical problem. In contrast, the CMD gives directly the values of σ_s and σ_φ for every meniscus profile, irrespective of whether these values are dynamic or equilibrium (relaxed).

(iv) The theory of elastic plates implicitly presumes a *closed* system, i.e. the lack of exchange of molecules between the interfacial layer and the bulk. This assumption is not fulfilled for a system with *adsorption dynamics*. In contrast, the CMD method proposed in the present article is applicable to both closed and open systems, just like the DSA for isotropic interfaces.

The CMD can considerably facilitate the formulation of an adequate rheological model for a given system. The CMD provides data not only for the drop/bubble profile, $r(z)$, but also for the two surface tensions, σ_s and σ_φ, as functions of the spatial coordinates and time. The CMD gives also the experimental functions $r(z)$, σ_s and σ_φ for the *initial* isotropic (or anisotropic) reference state, which is necessary for describing the system's evolution. This additional experimental information can be used for model discrimination and determining the best suited rheological model. As a first step, the applicability of a *purely elastic* model, like those in Refs. [19–23], could be tested. If the result is not satisfactory, one could further test a *viscoelastic* model, like the thixotropic model for protein adsorption layers in Refs. [46,47], having

determined the constant parameters of the model in advance, with a rotational rheometer.

6. Summary and conclusions

Here, we developed a method for determining the two components of the surface tension of axisymmetric drops and bubbles covered with anisotropic (solidified) adsorption layers. The method, called capillary meniscus dynamometry (CMD) is based on processing data not only for the digitized drop/bubble profile (as with DSA), but also for the instantaneous value of the capillary pressure of the drop/bubble, p_0. The principle of the CMD procedure for data processing is very different from that of the DSA. For DSA, the *whole* drop/bubble profile is fitted with the Laplace equation by adjusting two parameters, the surface tension and capillary pressure, using numerical minimization [24]. For CMD, the interface is split to small domains, and the meniscus shape in each domain is fitted with a quadratic curve. Then, applying the tangential and normal surface stress balance equations one determines the two components of the surface tension σ_s and σ_φ *locally*, in each of these surface domains. Numerical minimization is not used, so that the CMD computational procedure is fast and can be used to determine the surface-tension dynamics in real time during a given process.

An alternative approach exists, in which a rheological model of thin elastic plate is assumed from the very beginning [19–23]. However, in this case the obtained σ_s and σ_φ would depend on the choice of the rheological model and would represent theoretically calculated, rather than experimentally determined quantities. In contrast, by CMD σ_s and σ_φ are determined unambiguously from the experimental data for p_0 and the drop profile, without using any surface rheological model. Thus, σ_s and σ_φ can be considered as directly measurable quantities, which can be used for test of different rheological models. The values of σ_s and σ_φ could be not only *equilibrium* (for slow quasi-static processes), but also *dynamic* if the process is not too slow and the interfacial viscous stresses are essential.

Here, the CMD method is applied to determine σ_s and σ_φ during the evolution of a shrinking bubble that is formed on the tip of capillary in a solution of the protein HFBII hydrophobin. The results indicate that initially the surface tension is uniform and isotropic ($\sigma_s = \sigma_\varphi$). After a surface compression, σ_s and σ_φ become different and vary along the interface. After a subsequent compression, meridional wrinkles appear on the bubble surface, in a zone below the bubble "equator", where the azimuthal tension σ_φ takes negative values, in agreement with the theoretical predictions [49,50].

The CMD method (even without pressure measurements) is applicable also to the simpler case of isotropic fluid interfaces, for which it gives the same surface tension as the DSA and Wilhelmy plate methods. This has been verified by CMD experiments with water drops and bubbles in 100 mM aqueous SDS solution (Fig. 4); see also Fig. 6a, b and Table 1. However, the greatest advantage of the CMD is that it enables one to determine the tensions acting in anisotropic interfacial layers (membranes), like those formed from proteins, polymers, asphaltenes and phospholipids.

Acknowledgments

The authors gratefully acknowledge the support from Unilever R&D Vlaardingen; from the FP7 project Beyond-Everest, and from COST Actions CM1101 and MP1106. The authors are thankful to Dr. Jordan Petkov and Dr. Andrew Cox for the stimulating discussions.

Appendix A. The anisotropic interfaces are non-uniform and *vice versa*

Let us consider a general curved interface parameterized by curvilinear coordinates (u^1, u^2). The covariant derivative of the surface tension (stress) tensor reads [57]:

$$\sigma^\alpha_{\beta,\delta} = \frac{\partial \sigma^\alpha_\beta}{\partial u^\delta} + \Gamma^\alpha_{\gamma\delta}\sigma^\gamma_\beta - \Gamma^\gamma_{\beta\delta}\sigma^\alpha_\gamma \tag{A1}$$

Here, σ^α_β (α, $\beta = 1, 2$) are the components of the surface stress tensor; $\Gamma^\alpha_{\gamma\delta}$ is a Christoffel symbol of the second kind; all Greek indices take values 1 and 2, and summation is assumed over the repeated indices at different level. At equilibrium, the tangential projection of the surface *linear* momentum balance reads:

$$\sigma^\alpha_{\beta,\alpha} = 0 \tag{A2}$$

Eq. (A2) is a special case of Eq. (2.15) in Ref. [43] at negligible weight of the interface and bending moment effects. In the same approximation, the surface *angular* momentum balance, Eq. (2.30) in Ref. [43], implies that surface stress tensor is symmetric, so that it can be expressed in diagonal form in the eigenbasis:

$$\sigma^\alpha_\beta = \delta^\alpha_\beta \sigma^\alpha \tag{A3}$$

where δ^α_β is the Kronecker delta and σ^α ($\alpha = 1, 2$) are the eigenvalues of the surface stress tensor. In view of Eqs. (A1) and (A3), Eq. (A2) acquires the form:

$$\delta^\alpha_\beta \frac{\partial \sigma^\alpha}{\partial u^\alpha} + \Gamma^\alpha_{\beta\alpha}(\sigma^\beta - \sigma^\alpha) = 0 \tag{A4}$$

Setting $\beta = 1$ and $\beta = 2$ in Eq. (A4), we obtain the following two equations:

$$\frac{\partial \sigma^1}{\partial u^1} + \Gamma^2_{12}(\sigma^1 - \sigma^2) = 0 \tag{A5}$$

$$\frac{\partial \sigma^2}{\partial u^2} + \Gamma^1_{21}(\sigma^2 - \sigma^1) = 0 \tag{A6}$$

For curvilinear coordinates, Γ^2_{12} and Γ^1_{21} are (in general) different from zero. If the surface stresses are isotropic, $\sigma^1 = \sigma^2 = \sigma$, then Eqs. (A1) and (A2) imply that $\partial\sigma/\partial u^1 = 0$ and $\partial\sigma/\partial u^2 = 0$, i.e. σ is constant (uniform) throughout the surface. Conversely, if σ^1 and σ^2 are independent of u^1 and u^2, the derivatives in Eqs. (A5) and (A6) will be zero, and then it follows that $\sigma^1 = \sigma^2$. In other words, if the surface tension is isotropic, it is also uniform, and *vice versa*. The converse statement is also valid, viz. if the surface tension is anisotropic, it is also non-uniform, and *vice versa*.

Appendix B. Supplementary material

Supplementary data, viz. Appendix B "Derivation of the momentum balance equations for an axisymmetric meniscus"; Appendix C "Comparison of surface tensions measured by CMD and DSA", and Appendix D. "Application of CMD to bubble/wall interactions" associated with this article can be found, in the online version, at http://dx.doi.org/10.1016/j.jcis.2014.10.067.

References

[1] J.T. Petkov, T.D. Gurkov, B. Campbell, R.P. Borwankar, Langmuir 16 (2000) 3703–3711.
[2] R. Borbás, B.S. Murray, E. Kiss, Colloids Surf. A 213 (2003) 93–103.
[3] E.M. Freer, K.S. Yim, G.G. Fuller, C.J. Radke, Langmuir 20 (2004) 10159–10167.
[4] J. Krägel, S.R. Derkatch, R. Miller, Adv. Colloid Interface Sci. 144 (2008) 38–53.
[5] T.B.J. Blijdenstein, P.W.N. de Groot, S.D. Stoyanov, Soft Matter 6 (2010) 1799–1808.
[6] E. Aumaitre, S. Wongsuwarn, D. Rossetti, N.D. Hedges, A.R. Cox, D. Vella, P. Cicuta, Soft Matter 8 (2012) 1175–1183.

[7] G.M. Radulova, K. Golemanov, K.D. Danov, P.A. Kralchevsky, S.D. Stoyanov, L.N. Arnaudov, T.B.J. Blijdenstein, E.G. Pelan, A. Lips, Langmuir 28 (2012) 4168–4177.
[8] K.D. Danov, G.M. Radulova, P.A. Kralchevsky, K. Golemanov, S.D. Stoyanov, Faraday Discuss. 158 (2012) 195–221.
[9] V. Mitropoulos, A. Mütze, P. Fischer, Adv. Colloid Interface Sci. 206 (2014) 195–206.
[10] R. Stanimirova, K. Marinova, S. Tcholakova, N.D. Denkov, S. Stoyanov, E. Pelan, Langmuir 27 (2011) 12486–12498.
[11] G. Espinosa, D. Langevin, Langmuir 25 (2009) 12201–12207.
[12] L.R. Arriaga, F. Monroy, D. Langevin, EPL (Europhysics Letters) 98 (2012) 38007.
[13] N.-P.K. Humblet-Hua, E. van der Linden, L.M.C. Sagis, Soft Matter 9 (2013) 2154–2165.
[14] E.A. Evans, R. Skalak, CRC Crit. Rev. Bioeng. 3 (1979) 181–330.
[15] E. Hermans, J. Vermant, Soft Matter 10 (2014) 175–186.
[16] D.Y. Zang, E. Rio, D. Langevin, B. Wei, B.P. Binks, Euro. Phys. J. E 31 (2010) 125–134.
[17] G.G. Fuller, J. Vermant, Ann. Rev. Chem. Biomolec. Eng. 3 (2012) 519–543.
[18] Y. Fan, S. Simon, J. Sjöblom, Colloids Surf. A 366 (2010) 120–128.
[19] R. Long, K.R. Shull, C.-Y. Hui, J. Mech. Phys. Solids 58 (2010) 1225–1242.
[20] D. Carvajal, E.J. Laprade, K.J. Henderson, K.R. Shull, Soft Matter 7 (2011) 10508–10519.
[21] J.K. Ferri, P.A.L. Fernandes, J.T. McRuiz, F. Gambinossi, Soft Matter 8 (2012) 10352–10359.
[22] E.J. Laprade, R. Long, Langmuir 29 (2013) 1407–1419.
[23] S. Knoche, D. Vella, E. Aumaitre, P. Degen, H. Rehage, P. Cicuta, J. Kierfeld, Langmuir 29 (2013) 12463–12471.
[24] Y. Rotenberg, I. Boruvka, A.W. Neumann, J. Colloid Interface Sci. 93 (1983) 169–183.
[25] N.A. Alexandrov, K.G. Marinova, T.D. Gurkov, K.D. Danov, P.A. Kralchevsky, S.D. Stoyanov, T.B.J. Blijdenstein, L.N. Arnaudov, E.G. Pelan, A. Lips, J. Colloid Interface Sci. 376 (2012) 296–306.
[26] R.D. Stanimirova, K.G. Marinova, K.D. Danov, P.A. Kralchevsky, E.S. Basheva, S.D. Stoyanov, E.G. Pelan, Colloids Surf. A 457 (2014) 307–317.
[27] F. Bashforth, C. Adams, An Attempt to Test the Theories of Capillary Action, Cambridge Univ. Press, Cambridge, 1892.
[28] J.M. Andreas, E.A. Hauser, W.B. Tucker, J. Phys. Chem. 42 (1938) 1001–1019, http://dx.doi.org/10.1021/j100903a002.
[29] A.I. Rusanov, V.A. Prokhorov, Interfacial Tensiometry, Elsevier, Amsterdam, 1996.
[30] J.K. Ferri, S.Y. Lin, K.J. Stebe, J. Colloid Interface Sci. 241 (2001) 154–168.
[31] S.A. Zholob, A.V. Makievski, R. Miller, V.B. Fainerman, Adv. Colloid Interface Sci. 134 (2007) 322–329.
[32] F. Ravera, G. Loglio, V.I. Kovalchuk, Curr. Opin. Colloid Interface Sci. 15 (2010) 217–228.
[33] M. Hoorfar, A.W. Neumann, Adv. Colloid Interface Sci. 121 (2006) 25–49.
[34] A. Kalantarian, S.M.I. Saad, A.W. Neumann, Adv. Colloid Interface Sci. 199–200 (2013) 15–22.
[35] A. Passerone, L. Liggieri, N. Rando, F. Ravera, E. Ricci, J. Colloid Interface Sci. 146 (1991) 152–162.
[36] R. Nagarajan, D.T. Wasan, J. Colloid Interface Sci. 159 (1993) 164–173.
[37] C. MacLeod, C. Radke, J. Colloid Interface Sci. 160 (1993) 435–448.
[38] D.O. Johnson, K.J. Stebe, J. Colloid Interface Sci. 168 (1994) 21–31.
[39] A. Javadi, J. Krägel, M. Karbaschi, J. Won, A. Dan, G. Gochev, A.V. Makievski, G. Loglio, L. Liggieri, F. Ravera, N.M. Kovalchuk, M. Lotfi, V. Ulaganathan, V.I. Kovalchuk, R. Miller, in: P. Kralchevsky, R. Miller, F. Ravera (Eds.), Colloid and Interface Chemistry for Nanotechnology, CRC Press, Boca Raton, 2014. http://www.crcnetbase.com/doi/abs/10.1201/b15262-16.
[40] S.C. Russev, N. Alexandrov, K.G. Marinova, K.D. Danov, N.D. Denkov, L. Lyutov, V. Vulchev, C. Bilke-Krause, Rev. Sci. Instrum. 79 (2008) 104102.
[41] D. Georgieva, A. Cagna, D. Langevin, Soft Matter 5 (2009) 2063–2071.
[42] A. Javadi, J. Krägel, A.V. Makievski, N.M. Kovalchuk, V.I. Kovalchuk, N. Mucic, G. Loglio, P. Pandolfini, M. Karbaschi, R. Miller, Colloids Surf. A 407 (2012) 159–168.
[43] P.A. Kralchevsky, J. Eriksson, S. Ljunggren, Adv. Colloid Interface Sci. 48 (1994) 19–59.
[44] P.A. Kralchevsky, K. Nagayama, Particles at Fluid Interfaces and Membranes, Elsevier, Amsterdam, 2001. Chapters 3 and 4.
[45] M.B. Linder, Curr. Opin. Colloid Interface Sci. 14 (2009) 356–363.
[46] G.M. Radulova, K.D. Danov, Soft Matter 10 (2014) 5777–5786.
[47] K.D. Danov, P.A. Kralchevsky, G.M. Radulova, E.S. Basheva, S.D. Stoyanov, E.G. Pelan, Adv. Colloid Interface Sci. (2014), http://dx.doi.org/10.1016/j.cis.2014.04.009.
[48] X.L. Zhang, J. Penfold, R.K. Thomas, I.M. Tucker, J.T. Petkov, J. Bent, A. Cox, R.A. Campbell, Langmuir 27 (2011) 11316–11323.
[49] K.D. Danov, P.A. Kralchevsky, S.D. Stoyanov, Langmuir 26 (2010) 143–155.
[50] E.S. Basheva, P.A. Kralchevsky, N.C. Christov, K.D. Danov, S.D. Stoyanov, T.B.J. Blijdenstein, H.-J. Kim, E.G. Pelan, A. Lips, Langmuir 27 (2011) 2382–2392.
[51] M.H. Kutner, C.J. Nachtsheim, J. Neter, W. Li, Applied Linear Statistical Models, fifth ed., McGraw-Hill/Irwin, New York, 2005.
[52] E. Evans, D. Needham, J. Phys. Chem. 91 (1987) 4219–4228.
[53] V. Vitkova, J. Genova, I. Bivas, Eur. Biophys. J. 33 (2004) 706–714.
[54] W. Helfrich, R.-M. Servuss, Nuovo Cimento 3D (1984) 137–151.
[55] E. Evans, Adv. Colloid Interface Sci. 39 (1992) 103–128.
[56] L.M.C. Sagis, Rev. Mod. Phys. 83 (2011) 1367–1403.
[57] A.J. McConnell, Applications of Tensor Analysis (Dover Books on Mathematics), Dover Publications, New York, 2011.

Supplementary Material

for the article

Capillary meniscus dynamometry – method for determining the surface tension of drops and bubbles with isotropic and anisotropic surface stress distributions

by

Krassimir D. Danov, Rumyana D. Stanimirova, Peter A. Kralchevsky*, Krastanka G. Marinova, Nikola A. Alexandrov, Simeon D. Stoyanov, Theodorus B.J. Blijdenstein, Eddie G. Pelan

*Correspondence to: pk@lcpe.uni-sofia.bg

Contents Page

Appendix B. Derivation of the momentum balance equations for an axisymmetric meniscus

Let us parameterize the axisymmetric surface with curvilinear coordinates u^1 and u^2. It is convenient to introduce a Cartesian coordinate system, *Oxyz*, and a cylindrical coordinate system (r,φ,z) with *Oz* being the axis of revolution. As local surface basis, it is convenient to introduce curvilinear coordinates u^1 and u^2 as follows:

$$u^1 \equiv s\,, \quad u^2 \equiv \varphi \tag{B1}$$

where s is the arc length along the meniscus generatrix and φ is the azimuthal angle of the cylindrical coordinate system. The equation of the generatrix can be presented in a parametric form, viz. $r = r(s)$ and $z = z(s)$. Then, the following connections between the Cartesian and cylindrical coordinates take place over the meniscus:

$$x = r(u^1)\cos u^2\,, \quad y = r(u^1)\sin u^2\,, \quad z = z(u^1) \tag{B2}$$

Differentiating Eq. (B2), one obtains the vectors of the surface local covariant basis vectors, $\mathbf{a}_1$ and $\mathbf{a}_2$ [1,2]:

$$\mathbf{a}_1 = (\frac{\partial x}{\partial u^1}, \frac{\partial y}{\partial u^1}, \frac{\partial z}{\partial u^1}) = (\frac{\mathrm{d}r}{\mathrm{d}u^1}\cos u^2, \frac{\mathrm{d}r}{\mathrm{d}u^1}\sin u^2, \frac{\mathrm{d}z}{\mathrm{d}u^1}) \tag{B3}$$

$$\mathbf{a}_2 = (\frac{\partial x}{\partial u^2}, \frac{\partial y}{\partial u^2}, \frac{\partial z}{\partial u^2}) = (-r\sin u^2,\ r\cos u^2,\ 0) \tag{B4}$$

It is convenient to express the derivatives in Eq. (B3) through the meniscus slope angle θ:

$$\frac{\mathrm{d}r}{\mathrm{d}u^1} = \cos\theta, \quad \frac{\mathrm{d}z}{\mathrm{d}u^1} = \sin\theta \tag{B5}$$

Then, Eq. (B3) acquires the form:

$$\mathbf{a}_1 = (\cos\theta\cos u^2, \cos\theta\sin u^2,\ \sin\theta) \tag{B6}$$

From Eqs. (B4) and (B6) we obtain expressions for the components of the surface metric tensor, $a_{\alpha\beta} = \mathbf{a}_\alpha \cdot \mathbf{a}_\beta$ ($\alpha, \beta = 1, 2$), and for the running unit normal vector, $\mathbf{n}$:

$$a_{11} = 1, \quad a_{12} = a_{21} = 0, \quad a_{22} = r^2 \tag{B7}$$

$$\mathbf{n} = \frac{\mathbf{a}_1 \times \mathbf{a}_2}{|\,\mathbf{a}_1 \times \mathbf{a}_2\,|} = (-\sin\theta\cos u^2, -\sin\theta\sin u^2, \cos\theta) \tag{B8}$$

The surface contravariant basis vectors, $\mathbf{a}^1$ and $\mathbf{a}^2$, are collinear with $\mathbf{a}_1$ and $\mathbf{a}_2$, respectively. Moreover, we have $\mathbf{a}_\alpha \cdot \mathbf{a}^\beta = \delta_\alpha^\beta$, where the last symbol is the Kronecker delta. Then, knowing $\mathbf{a}_1$ and $\mathbf{a}_2$ we can easily find $\mathbf{a}^1$ and $\mathbf{a}^2$:

$$\mathbf{a}^1 = (\cos\theta\cos u^2, \cos\theta\sin u^2,\ \sin\theta) \tag{B9}$$

$$\mathbf{a}^2 = (-\frac{\sin u^2}{r}, \frac{\cos u^2}{r},\ 0) \tag{B10}$$

Consequently, the components of the contravariant metric tensor, $\mathbf{a}^{\alpha\beta} = \mathbf{a}^\alpha \cdot \mathbf{a}^\beta$ ($\alpha, \beta = 1, 2$), are:

$$a^{11}=1,\ \ a^{12}=a^{21}=0,\ \ a^{22}=1/r^2 \tag{B11}$$

To determine the Christoffel symbols, $\Gamma^{\mu}_{\alpha\beta}$ (α, β, μ = 1, 2), we have to calculate the following derivatives:

$$\frac{\partial \mathbf{a}_1}{\partial u^1}=(-\sin\theta\cos u^2\frac{\mathrm{d}\theta}{\mathrm{d}u^1},-\sin\theta\sin u^2\frac{\mathrm{d}\theta}{\mathrm{d}u^1},\cos\theta\frac{\mathrm{d}\theta}{\mathrm{d}u^1}) \tag{B12}$$

$$\frac{\partial \mathbf{a}_1}{\partial u^2}=(-\cos\theta\sin u^2,\cos\theta\cos u^2,0) \tag{B13}$$

$$\frac{\partial \mathbf{a}_2}{\partial u^1}=(-\cos\theta\sin u^2,\cos\theta\cos u^2,0) \tag{B14}$$

$$\frac{\partial \mathbf{a}_2}{\partial x^2}=(-r\cos x^2,-r\sin x^2,0) \tag{B15}$$

Thus, we obtain:

$$\Gamma^1_{11}=\frac{\partial \mathbf{a}_1}{\partial u^1}\cdot\mathbf{a}^1=0,\ \ \Gamma^1_{12}=\Gamma^1_{21}=\frac{\partial \mathbf{a}_1}{\partial u^2}\cdot\mathbf{a}^1=0,\ \ \Gamma^1_{22}=\frac{\partial \mathbf{a}_2}{\partial u^2}\cdot\mathbf{a}^1=-r\cos\theta \tag{B16}$$

$$\Gamma^2_{11}=\frac{\partial \mathbf{a}_1}{\partial u^1}\cdot\mathbf{a}^2=0,\ \ \Gamma^2_{12}=\Gamma^2_{21}=\frac{\partial \mathbf{a}_1}{\partial u^2}\cdot\mathbf{a}^2=\frac{\cos\theta}{r},\ \ \Gamma^2_{22}=\frac{\partial \mathbf{a}_2}{\partial u^2}\cdot\mathbf{a}^2=0 \tag{B17}$$

The covariant components $b_{\alpha\beta}$ (α, β = 1, 2) of the curvature tensor, **b**, are [1]:

$$b_{\alpha\beta}=\frac{\partial \mathbf{a}_\alpha}{\partial u^\beta}\cdot\mathbf{n} \tag{B18}$$

In view of Eqs. (B8) and (B12)–(B15), from Eq. (B18) we obtain:

$$b_{11}=\frac{\mathrm{d}\theta}{\mathrm{d}u^1},\ \ b_{12}=b_{21}=0,\ \ b_{22}=r\sin\theta \tag{B19}$$

In view of Eq. (B11), the mixed components of the curvature tensor, $b^{\beta}_{\alpha}=b_{\alpha\gamma}a^{\gamma\beta}$, are:

$$b_1^1 = \frac{\mathrm{d}\theta}{\mathrm{d}u^1}, \quad b_1^2 = b_2^1 = 0, \quad b_2^2 = \frac{\sin\theta}{r} \tag{B20}$$

At equilibrium, the local balance of the linear momentum at each point of the interface reads [3]:

$$\nabla_s \cdot \boldsymbol{\sigma} = p_s \mathbf{n} \tag{B21}$$

where $\boldsymbol{\sigma}$ is the surface stress tensor, ∇_s is the surface del operator, and p_s is the pressure difference across the interface; the effect of surface weight is neglected. If the effects of the surface bending moments are also negligible, then the tangential and normal projections of Eq. (B21) read:

$$\sigma^{\alpha}_{\beta,\alpha} = 0 \quad (\beta = 1,2) \tag{B22}$$

$$b^{\beta}_{\alpha}\sigma^{\alpha}_{\beta} = p_s \tag{B23}$$

As in Appendix A, here σ^{α}_{β} (α,β= 1,2) are the components of the surface stress tensor; all Greek indices take values 1 and 2, and summation is assumed over the repeated indices at different level. Eqs. (B22) and (B23) are special cases of Eqs. (2.15) and (2.16) in Ref. [3]. As shown in Appendix A, for β= 1, 2 Eq. (B22) reduces to

$$\frac{\partial\sigma^1}{\partial u^1} + \Gamma^2_{12}(\sigma^1 - \sigma^2) = 0 \tag{B24}$$

$$\frac{\partial\sigma^2}{\partial u^2} + \Gamma^1_{21}(\sigma^2 - \sigma^1) = 0 \tag{B25}$$

where σ^1 and σ^2 are the two eigenvalues of the surface stress tensor. Introducing the same notations as in the main text, $\sigma^1 = \sigma_s$, $\sigma^2 = \sigma_\varphi$, $u^1 = s$ and $u^2 = \varphi$, and substituting the Christoffel symbols from Eqs. (B16) and (B17), we bring Eqs. (B24) and (B25) in the form:

$$r\frac{\partial\sigma_s}{\partial r} + \sigma_s - \sigma_\varphi = 0, \qquad \frac{\partial\sigma_\varphi}{\partial\varphi} = 0 \tag{B26}$$

where we have used the relation $du^1 = ds = dr/\cos\theta$. The first equation in Eq. (B26) is identical to Eq. (2) in the main text. The second equation in Eq. (B26) is trivial because of the meniscus axial symmetry.

Furthermore, substituting σ_β^α from Eq. (A3) (Appendix A) and b_α^β from Eq. (B20) in the normal balance, Eq. (B23), we derive:

$$\sigma^1 \frac{d\theta}{du^1} + \sigma^2 \frac{\sin\theta}{r} = p_s \tag{B27}$$

Again, introducing the notations $\sigma^1 = \sigma_s$, $\sigma^2 = \sigma_\varphi$, $u^1 = s$ and $u^2 = \varphi$, and using Eq. (4), we obtain:

$$\kappa_s \sigma_s + \kappa_\varphi \sigma_\varphi = p_s \tag{B28}$$

which is Eq. (3) in the main text. Finally, utilizing again the relation $du^1 = ds = dr/\cos\theta$, we can bring Eq. (B27) in the form:

$$\sigma_s r \frac{d\sin\theta}{dr} + \sigma_\varphi \sin\theta = p_s r \tag{B29}$$

The substitution of σ_φ from Eq. (B26) into Eq. (B29) yields:

$$\sigma_s r \frac{d\sin\theta}{dr} + \sin\theta \frac{d}{dr}(\sigma_s r) = p_s r \tag{B30}$$

that is

$$\frac{d}{dr}(\sigma_s r \sin\theta) = p_s r \tag{B31}$$

The last equation coincides with Eq. (5) in the main text.

Appendix C. Comparison of surface tensions measured by CMD and DSA

C.1. Surface tension of a buoyant bubble

Fig. C1 shows the variation of the surface tension σ_{DSA} measured by the DSA method during the experiment described in Fig. 5 in the main article. The vertical arrows show moments in time t, at which video frames of the drop profile have been processed; see Fig. 5b in the main article. At t = 300 s, we have σ_{DSA} = 60.6 mN/m, which practically coincides with the value

σ = 60.8 mN/m determined by CMD; see Fig. 6b in the main paper, where it is demonstrated that the interface is still isotropic.

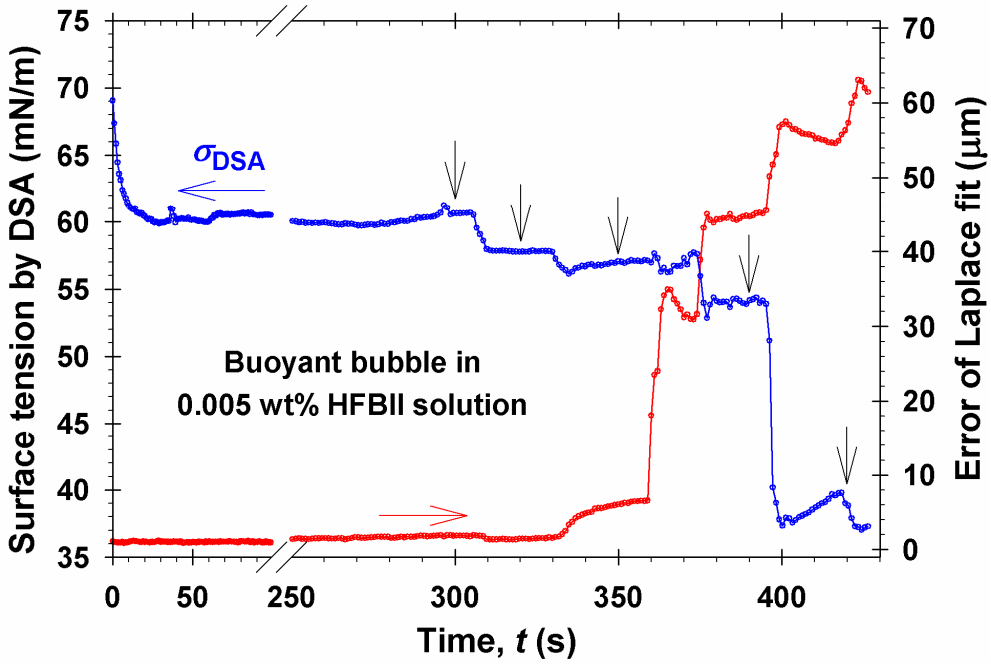

Fig. C1. Time dependencies of the surface tension σ_{DSA} and of the error of the Laplace fit given by the DSA apparatus for the experiment in Fig. 5 in the main article. The vertical arrows correspond to video frames with the bubble profile shown in Fig. 5b.

As seen in Figs. 6c,d and 7a,b (main paper), at t = 320 and 350 s the interface is already anisotropic. However, Fig. C1 shows that at t = 320 and 350 s the error of the Laplace fit is relatively small and it does not indicate that the surface solidification has happened. Rise of the error of the Laplace fit is observed at $t \geq 360$ s when the surface anisotropy has become significant; see Figs. 7c–f. As discussed in relation to Table 1 in the main text, at small deviations from isotropy the DSA can still fit the bubble/drop profile because there are two adjustable parameters, p_0 and σ. Thus, a good fit can be obtained at the cost of non-physical values of p_0 and σ, see Table 1 and Fig. 8 in the main text.

C.2. Surface tension of a pendant drop

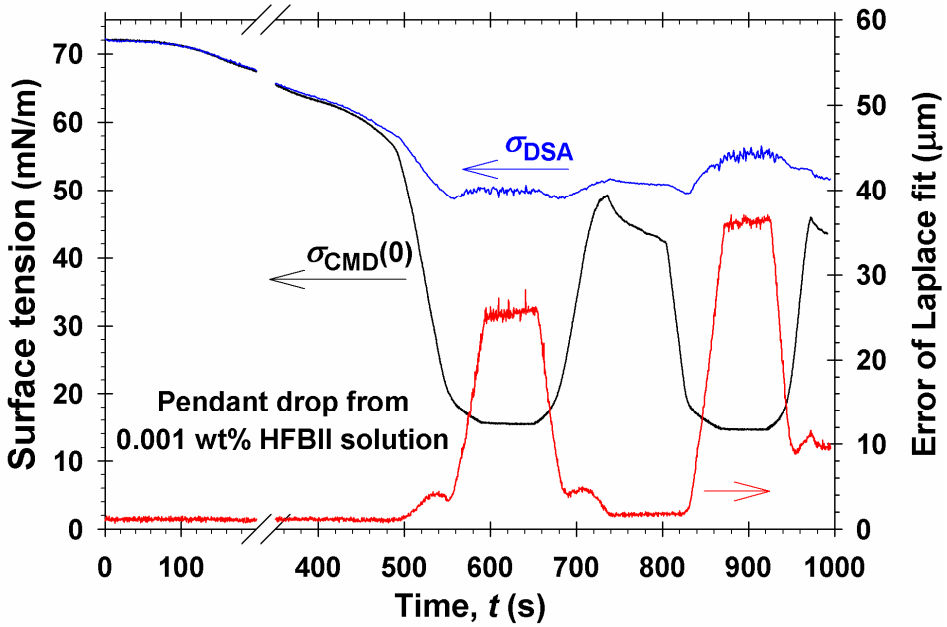

Fig. C2. Time dependencies of the surface tension σ_{DSA} and the error of the Laplace fit given by the DSA apparatus, as well as of the surface tension at the drop apex, $\sigma_{CMD}(0)$, measured by CMD. The data are for a pendant drop from 0.001 wt% HFBII solution.

Fig. C2 shows the variation of surface tension with time t for a pendant drop from 0.001 wt% HFBII. σ_{DSA} is the surface tension given by the DSA apparatus, and the error of the Laplace fit given by this apparatus is also plotted. Fig. C2 shows also the time dependence of the surface tension *at the drop apex*, where $\sigma_s = \sigma_\varphi \equiv \sigma_{CMD}(0)$, measured by CMD. To determine $\sigma_{CMD}(0)$, the curvature radius R_0 at the drop apex was determined by fitting the drop profile in this region with a circumference. In addition, the pressure p_0 was determined by pressure transducer (Fig. 3). Then, $\sigma_{CMD}(0) = p_0 R_0/2$.

For $t < 450$ s, the data in Fig. C2 indicate that $\sigma_{DSA} = \sigma_{CMD}(0)$, which means that the interfacial layer is isotropic. For $t > 450$ s, $\sigma_{CMD}(0)$ exhibits a minimum, a maximum and a second minimum, which are due to a consecutive compression, expansion and second compression of the bubble surface carried out by the experimentalist. The upper curve in Fig. C2 shows that σ_{DSA} has only small variations for $t > 450$ s, i.e. the DSA is insensitive to the interfacial compressions and expansions. The only indication for surface solidification is given by the error of the Laplace fit, which exhibits local maxima in the regions with the greatest

compressions. However, the most sensitive indicator for surface solidification is the difference between σ_{DSA} and $\sigma_{CMD}(0)$. At t = 900 s, σ_{DSA} = 55.3 mN/m, whereas $\sigma_{CMD}(0)$ = 14.7, so that this difference reaches 40.6 mN/m (Fig. C2).

Appendix D. Application of CMD to bubble/wall interactions

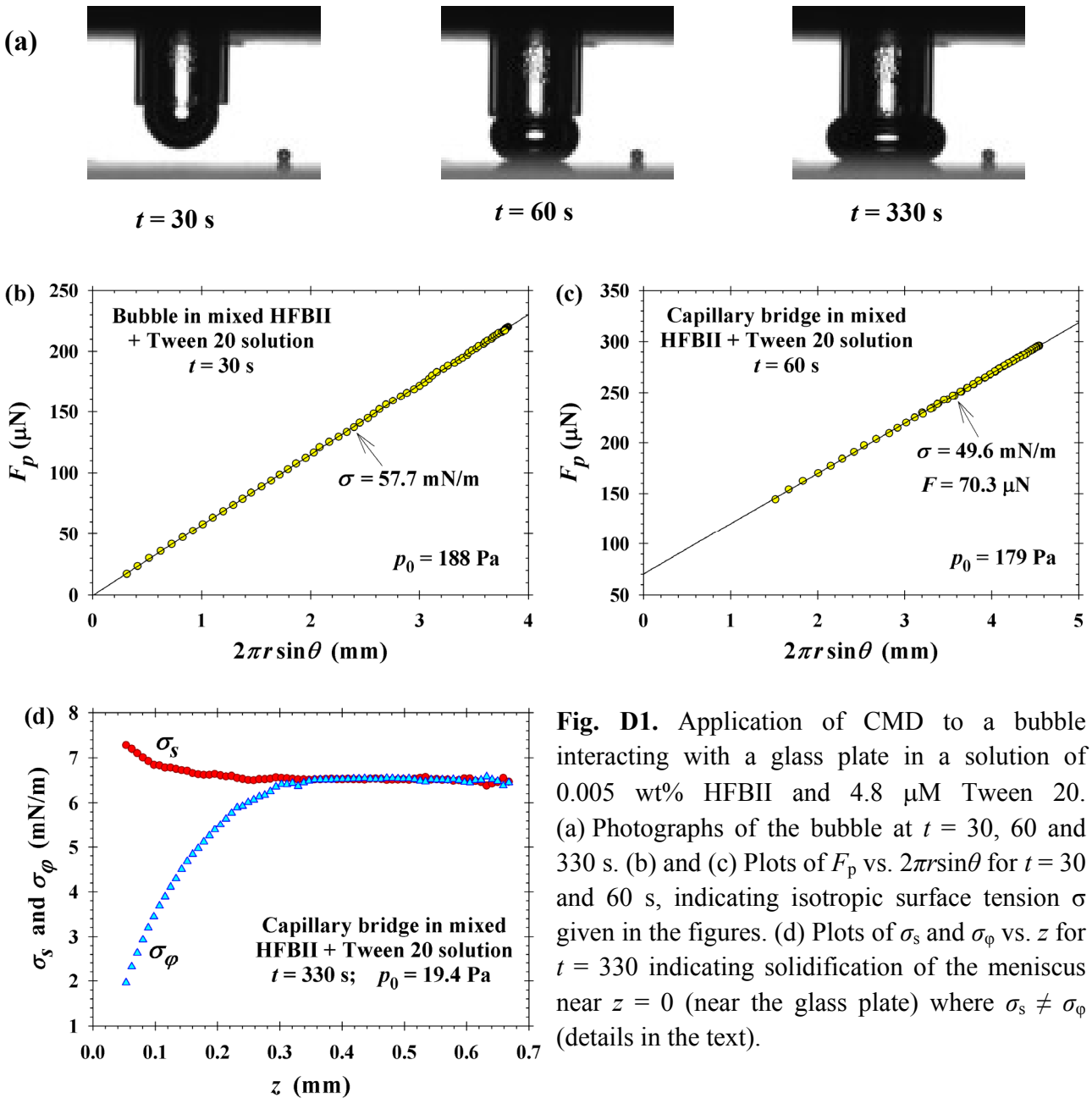

Fig. D1. Application of CMD to a bubble interacting with a glass plate in a solution of 0.005 wt% HFBII and 4.8 μM Tween 20. (a) Photographs of the bubble at t = 30, 60 and 330 s. (b) and (c) Plots of F_p vs. $2\pi r\sin\theta$ for t = 30 and 60 s, indicating isotropic surface tension σ given in the figures. (d) Plots of σ_s and σ_φ vs. z for t = 330 indicating solidification of the meniscus near z = 0 (near the glass plate) where $\sigma_s \neq \sigma_\varphi$ (details in the text).

Fig. D1a shows three consecutive video frames of an air bubble formed at the tip of a capillary in a mixed solution of the protein hydrophobin HFBII and the nonionic surfactant Tween 20. The bubble is pressed against a horizontal glass plate immersed in the solution.

In the moment of time t = 30 s, the bubble is not yet in contact with the glass plate (Fig. D1a). From the digitized profile of the bubble surface and from the pressure p_0 = 188 Pa measured by the pressure transducer we determined the pressure force F_p and plotted it vs. $2\pi r\sin\theta$; see Fig. D1b. The plot is a straight line through the coordinate origin, which indicates isotropic surface tension, just like in Figs. 6a and b in the main article. The slope of this linear dependence, σ = 57.7 mN/m, yields the value of the surface tension in view of Eq. (11) in the main article.

At t = 60 s, the bubble is already pressed against the glass plate (Fig. D1a, the photo in the middle). As above, from the digitized profile of the bubble surface and from the pressure p_0 = 179 Pa measured by the pressure transducer we determined the pressure force F_p and plotted it vs. $2\pi r\sin\theta$; see Fig. D1c. Again, the plot is a straight line, which indicates isotropic surface tension. In this case, the bubble forms a capillary bridge between the capillary tube and the plate. The *capillary bridge force* between the bubble and the plate, F, equals the difference between the forces due to pressure and surface tension [4]. Then, instead of Eq. (11), we have:

$$F_p = 2\pi r\sigma_s \sin\theta + F \tag{D1}$$

In view of Eq. (D1), from the slope and the intercept of the plot in Fig. D1c we determine σ = 49.6 mN/m and F = 70.3 μN. The positive value of F corresponds to repulsion between the capillary tube and the plate, mediated by the bubble that represents a capillary bridge.

After pressing the bubble against the plate and waiting for a certain period of time, the pressure in the bubble is decreased (by sucking air through the capillary), which gives rise to a process of gentle bubble detachment from the substrate. The bubble profile at t = 330 s (corresponding to a lower pressure, p_0 = 19.4 Pa) is shown in the rightmost photo in Fig. D1a. In this case, the plot of F_p vs. $2\pi r\sin\theta$ is not a straight line, which indicates solidification of the interfacial layer. For this reason, we applied the complete CMD procedure from Section 3 and determined the variations of the two surface tensions, σ_s and σ_φ, which are shown in Fig. D1d as functions of the vertical coordinate, z. The coordinate origin, z = 0, corresponds to the surface of

the glass plate. The upper part of the bridging bubble, for $z > 3.4$ mm, the two surface tensions coincide, $\sigma_s = \sigma_\varphi = 6.52$ mN/m, so that in this part of the bubble the surface tension is isotropic. In contrast, for $z < 3.4$ mm, we obtain $\sigma_\varphi < \sigma_s$, i.e. in the lower part of the bubble, near the substrate, the surface tension is anisotropic. The smaller values of σ_φ can be explained with the shrinking of the bubble surface after sucking of gas from its interior. The results in Fig. D1d indicate that this shrinking happens mostly in the lower part of the bubble, in azimuthal direction. The slightly greater values of σ_s in this region indicate a slight extension of bubble surface in vertical direction, which is related to the onset of bubble detachment from the substrate upon decreasing its volume. For a more systematic study on the application of CMC to investigate the adhesion of bubbles and drops to solid surfaces see Ref. [5].

References

[1] A.J. McConnell, Applications of Tensor Analysis (Dover Books on Mathematics), Dover Publications, New York, 2011.

[2] G.A. Korn, T.M. Korn, Mathematical Handbook for Scientists and Engineers: Definitions, Theorems, and Formulas for Reference and Review, Dover Publications, New York, 2000.

[3] P.A. Kralchevsky, J. Eriksson, S. Ljunggren, Adv. Colloid Interface Sci. 48 (1994) 19–59.

[4] P.A. Kralchevsky, K. Nagayama, Particles at Fluid Interfaces, Elsevier, Amsterdam, 2001; Chapter 11.

[5] K.D. Danov, R.D. Stanimirova, P.A. Kralchevsky, K.G. Marinova, S.D. Stoyanov, T.B.J. Blijdenstein, E.G. Pelan et al., manuscript in preparation.